

1 **Influence of surface roughness on the sputter yield of Mo under**
2 **keV D ion irradiation**

3

4 M. Kelemen^{1,2}, T. Schwarz-Selinger³, A. Mutzke⁴, M. Balden³,
5 E. Vassallo⁵, M. Pedroni⁵, D. Dellasega^{5,6}, M. Passoni^{5,6},
6 F.Romeo^{5,6}, A. Hakola⁷, P. Pelicon¹, R. Zaplotnik¹ and S.
7 Markelj¹

8

9 ¹ Jožef Stefan Institute, Jamova 39, SI-1000 Ljubljana, Slovenia

10 ² Jožef Stefan International Postgraduate School, Jamova cesta 39, 1000 Ljubljana, Slovenia

11 ³ Max-Planck-Institut für Plasmaphysik, Boltzmannstrasse 2, D-85748 Garching, Germany

12 ⁴ Max-Planck-Institut für Plasmaphysik, Wendelsteinstrasse 1, D-17491 Greifswald, Germany

13 ⁵ Istituto per la Scienza e Tecnologia dei Plasmi CNR, Via Roberto Cozzi, 53-20125 Milano, Italy

14 ⁶ Politecnico di Milano, via Ponzio 34/3, 20133 Milan, Italy

15 ⁷ VTT Technical Research Centre of Finland Ltd, P O Box 1000, FI-02044, VTT, Finland

16

17 ***Corresponding author: M. Kelemen**

18 E-mail address: mitja.kelemen@ijs.si

19 **Abstract**

20 In this work the influence of surface roughness on the sputter yield of Mo under
21 keV D ion bombardment was investigated for different impact angles. For this
22 purpose, thin films of Mo (~ 120 nm) were deposited by pulsed laser deposition onto
23 graphite substrates with varying surface roughness (Ra ranging from 5 nm to 2-
24 3 μm). The as-deposited samples were irradiated at room temperature by 3 keV D₃⁺
25 ions originating from an electron cyclotron resonance ion gun. Samples were
26 exposed to D ions at angles between 0° and 70° and fluences in range of 10²³ D/m².
27 The areal densities of the Mo marker layers were determined with Rutherford-
28 backscattering spectroscopy. For all the surfaces we observed a strong angular
29 dependence of the sputter yield. For smooth and intermediate surface roughnesses,
30 up to Ra ~ 280 nm, we obtained an increase of the sputter yield with the angle up to
31 a factor of five compared to 0°. In contrast, at the highest surface roughness in the 2-
32 3 μm range the sputtering yield decreases with increasing impact angle. The
33 obtained data were compared to SDTrimSP-3D simulations. We obtained good
34 agreement between the simulated and experimental sputter yield for surfaces for
35 which we could provide high resolution atomic force microscopy (AFM) surface
36 representations. As high-resolution surface mapping was not possible for surface
37 roughness of 2-3 μm, we found large deviation between the calculation and the
38 measured data. The combination of measured and simulated data represent
39 important input for predicting the erosion rates of surfaces in inner walls of
40 thermonuclear fusion devices, which are expected to change surface roughness over
41 time by sustained plasma exposure.

42

43 *Keywords:* Ion beam, Deuterium, RBS, Sputter yield, surface roughness, angular
44 dependence

45

46 **Introduction**

47 An important issue in the development of thermonuclear fusion reactors is the
48 lifetime of the reactor wall. Bombardment by energetic ions and neutrals from the
49 plasma will lead to continuous erosion of the plasma-facing surface. In addition, the
50 eroded material can contaminate the core plasma. Inside the plasma chamber of a
51 fusion device, particles coming from the plasma impinge on the components at
52 different angles depending on both local plasma parameters and on the orientation
53 of the magnetic fields lines, which roughly guide the charged particles from plasma
54 to the surface of the inner wall material. For instance at the components in the
55 divertor region, the magnetic field lines intersect the target plate surface at shallow
56 incidence angles of a few degrees. The particles impact at average angles of
57 around 60°, with some angular distribution, due to the additional effect of the sheath
58 potential on the ion trajectories close to the surface and additional gyration of ions in
59 magnetic field [1].

60 Many studies have been carried out to determine the sputter yield on smooth
61 surfaces in varying combinations of projectile ions and target atoms at different
62 impact energies and impact angles. The major results are summarised in the work of
63 *R. Behrisch and W. Eckstein* [2]. There a distinct angular dependence of the sputter
64 yield is observed [2]. However, for rough surfaces the angular dependence can
65 behave in an unexpected way [3-6] and most of the past work was done for materials
66 (B, Fe), which are not presently foreseen in future fusion devices as plasma-facing
67 materials. In general, the plasma-facing components (PFC) in a fusion device, which
68 are affected by the highest particle fluxes (divertor), are made out of heavy refractory
69 metals such as tungsten (W) [7]. For this reason, comparison between data
70 extracted from well-defined laboratory experiments and results obtained in fusion
71 devices is needed. In this paper we will concentrate on the first part.

72

73 The main goal of this study is to investigate the effect of surface roughness on
74 sputter yield at different impact angles to improve the quality of the available data. In
75 the past, some effort has been spent on the quantification of the sputter yields on
76 rough surfaces in set-ups where a light projectile (H or D) impacted on a heavy
77 target atom (heavier than Fe) [4,9]. Part of that work was focused on providing
78 validation data for the development of computer codes such as SDTrimSP-3D [9]
79 and TRI3DYN [8]. In the past studies, samples with well-defined surface topography
80 and small values of surface roughness (up to 20 nm [5]) have been used. Data
81 obtained in those studies are valuable for verifying the predictive quality of simulation
82 codes. However, they are not representative for the surface topography of PFCs in a
83 tokamak environment, which generally exhibit much higher roughness, even in their
84 virgin condition as delivered from the material production line. To address this gap,
85 we have decided to study erosion of thin Mo films on graphite substrate with varying
86 degrees of surface roughness typical for tokamak PFCs. This study is a precursor for
87 exposures in tokamak devices on similar surfaces. These tests are envisaged in
88 ASDEX Upgrade (AUG). As AUG is a full W machine, the deposition of W from other
89 plasma-facing components is unavoidable. To be able to observe the sputtering in
90 AUG, a proxy material for W has to be chosen. Mo was chosen as both materials
91 show similar behaviour of sputter yield under keV D ion bombardment [1,8], at least
92 for smooth surfaces at 0° impact angle. The main difference is in absolute values of
93 sputter yields and sputter threshold energy. The particle energies hitting the PFCs in
94 a fusion device are predominately ions in the eV energy range, however some
95 particles can reach keV energies. As most of the light particles (D, T, He) will have
96 energies even below the sputter threshold [2], sputtering will be dominated by the
97 high energy ions and neutrals originating from core plasma.. High energy particles
98 are produced by instabilities of core plasma as response to different mechanism of
99 heating the plasma. Additional some energetic particles are produced in charge

100 exchange reactions, which are able to reached the reactor inner wall. For this reason
101 we have decided to study the effect of sputter yield on surface roughness in keV
102 energy range.

103 We used 115-120 nm thick Mo films deposited by pulsed laser deposition on
104 textured graphite substrates of varying surfaces roughness. The samples were
105 exposed to D ions with energy of 1 keV/D, under impact angles between 0° and 70°.
106 The erosion was characterised using Rutherford Backscattering Spectroscopy (RBS)
107 as the main analysis tool. The surface morphology was carefully analysed with
108 atomic force microscopy (AFM), confocal laser scanning microscopy (CLSM) and
109 scanning electron microscopy (SEM). Finally, SDTrimSP-3D simulations were
110 performed and will be compared to the experimental data.

111

112 **2. Sample preparation and characterization**

113 For all studied samples, fine-grained graphite was used as substrate. The
114 graphite was cut into 4 mm thick pieces of dimensions of 15×16 mm². Samples with
115 four different surface roughness were prepared. As a measure for the surface
116 roughness, we took the arithmetic average deviation from the average surface
117 height, Ra, as measured by AFM or CLSM. The surface roughness of the samples
118 ranged from polished surfaces (Ra~5 nm) up to very rough surfaces (Ra~2-3 μm,
119 typical for a surface after machining), with two intermediate roughness steps of
120 Ra~110 nm and Ra~280 nm. The samples were first polished to a surface
121 roughness of Ra~5 nm, as measured with AFM, on a micrometer lateral scale. Fine
122 grain graphite poses unique challenges during its polishing. Due to its grainy
123 structure, some grains fell out during the polishing and the subsequent cleaning. This
124 results many micrometer holes on the surface in the overall smooth surface. These
125 influence the results, which will be elaborated in the discussion part of the paper.

126

127 Part of the polished substrates were then treated with plasma etching by
128 exposing them to a plasma consisting of a mixture of CF_4 and H_2 gas at 9 Pa, driven
129 with a 13.56 MHz RF power supply. To achieve $R_a \sim 110$ nm, samples were exposed
130 for 25 min at a discharge voltage of 750 V, while for $R_a \sim 280$ nm the exposure time
131 was increased to 90 min and the discharge voltage to 850 V [10]. An example of
132 AFM topographical maps for a sample with surface roughness of 110 nm (Mo 065) is
133 presented in Figure 1a. From this AFM data, we can determine the height distribution
134 of the samples surface, shown in Figure 1b and also the distribution function of
135 surface angles, shown in Figure 1c. To produce samples with an even higher surface
136 roughness above $1 \mu\text{m}$, the substrate was sandblasted with glass spheres, using a
137 driving pressure of 3 bar. To determine the surface roughness of this sample type,
138 we performed CLSM on the finished sample after texturing and Mo coating. The
139 obtained surface roughness was in the range of $R_a \sim 2\text{-}3 \mu\text{m}$, with some significant
140 variation between samples and different points on sample.

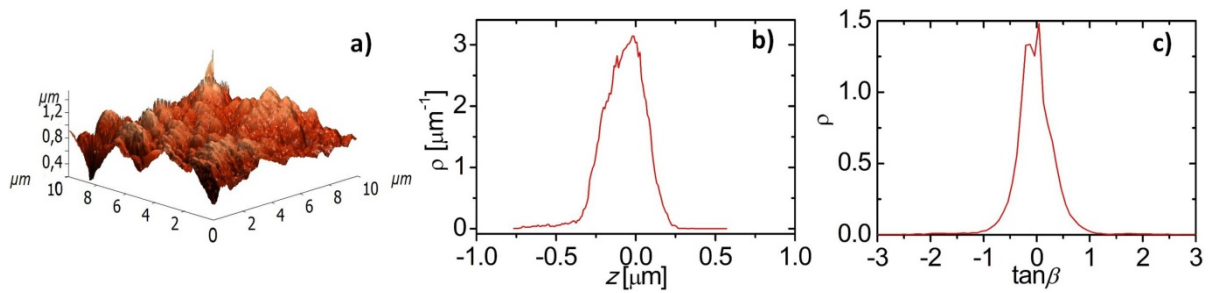
141

142 The prepared substrates were coated with a thin film of Mo (thickness 115-120
143 nm), using pulsed laser deposition in vacuum. The laser fluence was 2 J/cm^2 and the
144 deposition time 11 minutes. Thanks to the high energy of impinging species, the
145 deposited films mimic the surface morphology of the treated substrate while ensuring
146 a good adhesion. A uniform coverage of Mo over the whole sample surface was
147 obtained by rotating the substrate holder. The uniformity of the Mo coatings was
148 checked by SEM and RBS with ^4He ions before exposure to D ion irradiation. In
149 figure 2, we show the SEM images of graphite substrates for a polished, for one of
150 the intermediate roughness steps and for a $2\text{-}3 \mu\text{m}$ rough surface, before and after
151 coating it with Mo. From the presented data, we can conclude that the coverage of
152 Mo is rather uniform and that the deposition has not significantly altered the surface

153 morphology of the substrates. The RBS spectra support this conclusion as no
 154 change in the low energy shoulder of the Mo peak is visible.

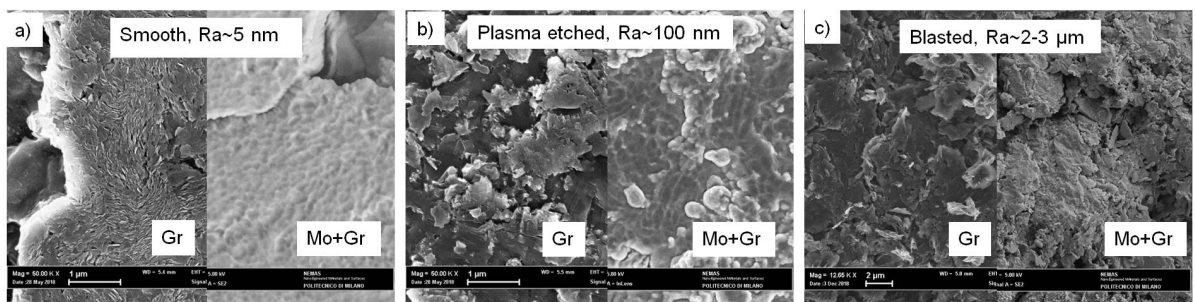
155

156 The chosen exposure fluence of D ions for the sputter yield measurements was
 157 sufficiently low that D ions did not introduce additional features on the samples. This
 158 can be seen in Figure 3 showing CLSM microscopy images as well as surface height
 159 for the sample with a 2-3 μm roughness for both the virgin sample and after the D
 160 ion exposure in the centre of the sputtering crater. No apparent differences show up,
 161 considering that in the extreme cases we erode 1/3 of the original Mo layer
 162 thickness.



163

Figure 1: AFM image of Mo 065 sample with surface roughness of $R_a \sim 110$ nm (a). From AFM images we extracted distribution density - ρ for height - z (b) and slope angles - β (c), respectively.



164

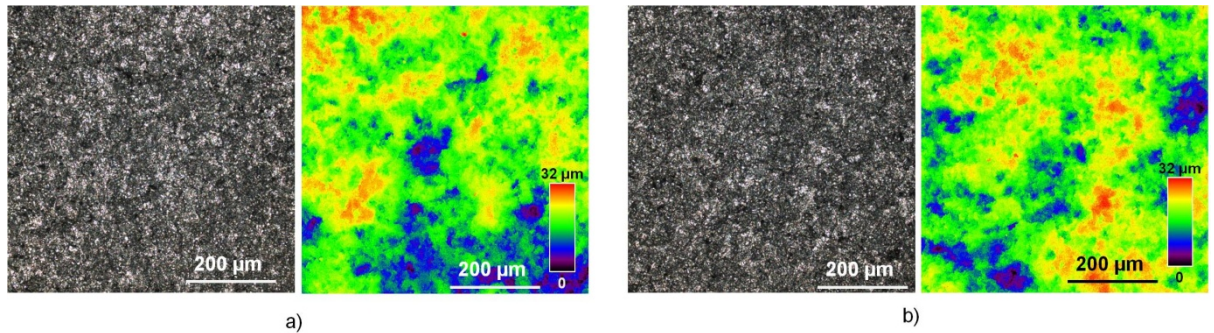
165

Figure 2: SEM images of secondary electrons from graphite samples with surface roughness (a) 5 nm, (b) 110 nm and (c) 2-3 μm after surface treatment. The left images show the graphite substrate (Gr) and right ones after the deposition of ~ 120 nm Mo coating (Mo-Gr).

166

167

168



169

Figure 3: CLSM images of a sample with a surface roughness of $Ra \sim 2-3 \mu m$ (sample Mo 075). a) virgin sample, b) near the centre of the sputtering crater after D ion exposure. Left is the composite light image of z scan, right is the height distribution of the surface.

170

All the samples were analysed by RBS using a ^4He ion beam at 2.5 MeV before and after exposure to the D ion beam. From RBS, the areal density of the Mo layer can be obtained, which is often for convenience transformed into an equivalent layer thickness value using the theoretical Mo bulk atomic density. We used the SIMNRA software [11] to obtain the areal density. All measurements were performed in the INSIBA experimental chamber coupled to the 2 MV tandem accelerator at Jožef Stefan Institute (JSI) [13]. For the detection of the backscattered He ions in the RBS measurements, we used a Passivated Implanted Planar Silicon (PIPS) detector installed at 165° scattering angle with a circular aperture with a diameter of 5.7 mm, corresponding to a solid angle of 0.689 msr. The schematic representation of the RBS measurement set-up is shown in Figure 4b. The deposited dose of ^4He ions was controlled by integrating the beam current on a mesh charge collector mounted between the collimating slits and the sample [12]. With the ^4He probing beam, we performed a lateral scan in the middle of the sample in the direction of the rotation axis to avoid geometric effects of the D beam projection on the sample at different impact angles. For the RBS analysis, we used a probing beam with a diameter of 1 mm. The measurements were performed in 2 mm lateral steps.

187

188

3. Experimental set-up for sputter yield measurements

We designed a special experimental set-up to perform the study of sputter yield as a function of the impact angle. This set-up was mounted inside the INSIBA vacuum chamber [13], where a newly constructed sample holder was mounted for this study. This holder allows rotating samples up to 90° with respect the ion beam axis, where the vertical Z axis on the sample is our rotation axis. The normal of the sample is defined as Y axis and together with the axis of the ion gun they define the impact angle of the ion beam. The experimental set-up is schematically represented

in Figure 4a.

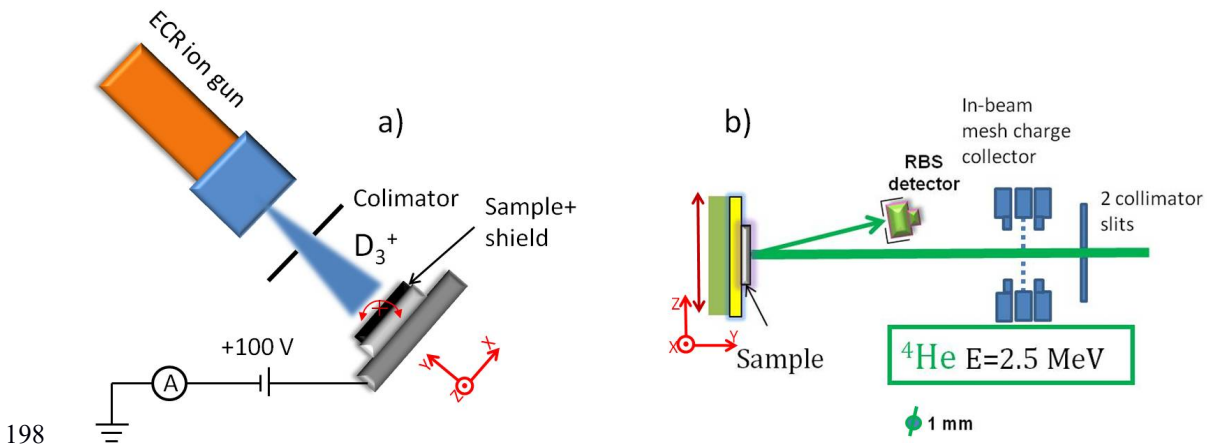


Figure 4: Top views of experimental set-ups for a) D ion irradiation at different impact angles (rotation axis represented by red cross) and b) RBS measurement for characterisation of samples (scanning direction marked by red arrow is along rotation axis in a)). Both set-ups can't be installed in the INSIBA experimental chamber simultaneously, therefore we had to use them interchangeably [13].

Additionally, we added a special shield for the side faces of the samples. The shield was made of stainless steel to prevent unintended sputtering of the edges of the graphite substrate at higher impact angles and redeposition of carbon on the Mo surface. A commercial Electron Cyclotron Resonance (ECR) ion gun (IonEtch Gen II made by Tectra GmbH) was used as a source for the keV D ions. The ECR ion source uses microwaves at a frequency of 2.45 GHz to excite gas inside the plasma chamber surrounded by rare earth permanent magnets providing the magnetic field

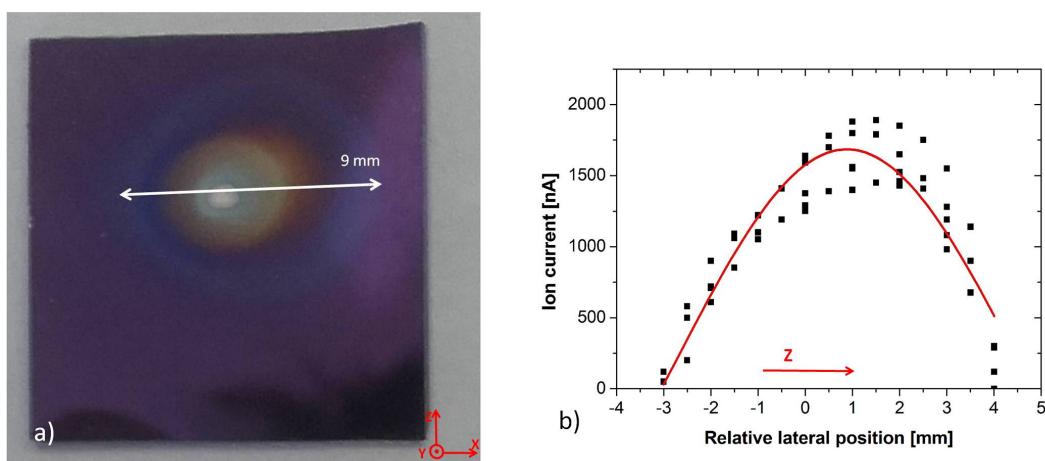
206 to maintain the plasma in the chamber. The ions are accelerated by applying a
207 voltage to the extraction electrode in the excitation chamber. In our experiment we
208 used D₂ feeding gas to produce D ions. To run the D plasma, the pressure in the
209 INSIBA vacuum chamber typically increased to 30 mPa nitrogen equivalent. At such
210 conditions, the dominant species extracted from the plasma chamber are D₃⁺ (about
211 93 %) [12]. The ion flux was monitored by measuring the ion current on the sample
212 during the exposure experiment. To suppress secondary electrons escaping from the
213 sample, the rotatable sample holder was biased to +100 V. The positive extraction
214 voltage of the ion gun was adjusted to 3.1 kV resulting in an ion energy of 3 keV. We
215 assume that for molecular ions (D₃⁺, D₂⁺) the energy is shared evenly between the D
216 atoms upon contact with the sample surface. Thus, the D flux is nearly three times
217 larger than the measured ion flux and we refer to these conditions as 1 keV/D for the
218 majority D₃⁺ ions impacting on the surface.

219 The D ion beam at the exit of the ECR gun has a large angular divergence,
220 which is energy dependent. For our applied extraction voltage of 3.1 kV, the beam
221 average divergence angle is $\approx 30^\circ$ [14]. Due to a relatively large distance between
222 the sample and the ECR ion gun exit aperture of 33 mm, a large fraction of the beam
223 would not only hit the sample but also the supporting structure of the rotating table.
224 In this case, we would still measure these ions as ion current, while they would not
225 contribute to the erosion of Mo and consequently overestimate the real sputter yield.
226 To overcome this issue and to produce a well-defined ion beam size at the sample
227 position, we inserted a molybdenum collimating aperture of 2.7 mm in diameter
228 between the ECR source and the sample, which is positioned between the source
229 and the sample, 28.2 mm in front of it. This reduced the beam diameter to a value
230 below the lateral sample size at 0° impact angle. Since at higher impact angles the
231 beam diameter is geometrically enlarged, still a part of the beam misses the sample.
232 Due to well-done calibration of the ion gun output, the ion current measurements

233 during the exposure were only used to control the stability of ion gun output over the
234 time of exposure, as it can drift over longer times due to change of the pressure in
235 plasma chamber of the ion gun. The ion fluence at the RBS analysing position was
236 calculated from the average ion gun output as measured during the calibration
237 process.

238

239 The ion beam size and the profile at the sample position were measured by two
240 independent methods. One was by eroding a thin film of amorphous hydrocarbon (a-
241 C:H) layer on silicon. The beam size and the erosion crater were derived by optical
242 interference of the light on the thin film as seen in Figure 5a.



243

Figure 5: a) Image of the erosion crater, created by 1 keV/D ions, as seen on a thin a-C:H film on silicon. b) lateral profile along the sample rotation axis of the 1 keV/D ion beam as measured using a Faraday cup with a 2 mm aperture. Due to geometrical constraints in the experimental chamber, the distance from collimator to the Faraday cup aperture is reduced to 20.2 mm instead of 28.2 mm where the surface of exposed samples was later positioned.

244 Secondly, we carried out lateral scans of the ion current with a Faraday cup
245 along the Z axis. The results of the scans are shown in Figure 5b. The Faraday cup
246 had an entrance hole of 2 mm in diameter and the current measurements were
247 made at a distance of 20.2 mm from the collimating aperture, instead of 28.2 mm
248 where surface of the exposed samples was. By the Z axis scans we confirmed that
249 90% of the total ion current is within a nominal beam diameter of 6.7 mm. If one

250 corrects the difference in the distances between the Faraday cup during the current
251 measurements and the a-C:H sample, we obtain a value of 9.4 mm for the beam
252 diameter at the sample position. Both methods give a good agreement in D ion beam
253 size, which we estimate to be 9 mm in diameter. The ion beam exhibits a truncated
254 Gaussian profile. The central maximum of the D ion beam flux was determined to be
255 8×10^{18} D ions/m²s with the Faraday cup measurements. By averaging the ion flux
256 as measured by the Faraday cup over the entire irradiated area, we end up with an
257 average flux of around 3×10^{18} D ions/m²s. The total D ion current impinging on the
258 sample was measured during the irradiation with a Keithley 2000 multimeter. The
259 time average fluence per sample was calculated as the time integral of the D ion
260 current divided by the beam area and elementary electron charge and multiplied by
261 three due to the D₃⁺ ions. This laterally averaged fluence is suitable to compare
262 experiments during the exposure and for monitoring the stability of the D ion beam.
263 However, to derive the sputter yield the maximum fluence of the exposure spot was
264 used and compared with the maximum erosion derived from RBS as will be
265 explained in the result section.

266

267 **4. SDTrimSP-3D simulations**

268 The angle-dependent sputter yield measurements were compared with static
269 SDTrimSP-3D [9] simulations based on the sample surface morphology extracted
270 from AFM scans and CLSM microscopy. For samples with intermediate roughness
271 AFM measurements on 10×10 μm² grid with lateral resolution of 39 nm and high
272 resolution of less than 1 nm. For the roughest samples surface height measurements
273 performed with CLSM microscope on 650×650 μm² grid with lateral resolution of 625
274 nm high resolution of less than 100 nm. Those data were used as input for
275 SDTrimSP-3D simulations with linear interpolation between measuring points to

276 match the surface cell density in SDTrimSP-3D grid with periodic boundary condi-
277 tions.

278

279 **5. Results and discussion**

280 5.1 Experimental results

281 The samples were irradiated with a maximum fluence of the exposure spot
282 ranging from 0.85 to 3.19×10^{23} D ions/m² at different impact angles of 0°, 40°, 60°
283 and 70°. A detailed list of irradiation parameters for each individual sample can be
284 found in Table 1. Initially it was planned to erode 10-20 % of the initial layer and we
285 calculated that for this we would need a fluence of approximately 2×10^{23} D ions/m².
286 However, since we expected a strong dependence of the sputter yield on the
287 exposure angle [2, 4] we needed to adjust the exposure fluence for some exposure
288 conditions not to erode too much of the initial layer. Still, due to the large variation of
289 the sputter yield in some cases up to 50 % of the initial layer was eroded. Besides
290 this upper limit for the D fluence we kept a lower fluence limit for all irradiations.
291 Recent experiments showed a fluence dependent sputter yield for D ion irradiation of
292 iron [6]. However, the effect becomes noticeable only at fluence values below
293 10^{22} ions/m² and can be attributed to the presence of oxides at the surface. For
294 monoelemental surfaces without surface oxide layer, this threshold fluence should
295 be even lower, as shown for iron targets [15]. For this reason, we assume that the
296 different exposure fluences applied in our experiment on different samples do not
297 significantly influence the obtained sputter yield values.

298

299

300

Sample	Treatment	Ra	Angle	Maximum	Sputter yield
--------	-----------	----	-------	---------	---------------

		[nm]	[°]	fluence [*10 ²³ D/m ²]	[*10 ⁻² Mo/D]
Mo061	Polishing	~5	0	2.67	0.6±0.15
Mo062	Polishing	~5	40	3.19	1.0±0.3
Mo063	Polishing	~5	60	2.53	1.6±0.60
Mo064	Polishing	~5	70	1.39	2.5±1.0
Mo065	Plasma etching	~110	0	2.46	0.5±0.1
Mo066	Plasma etching	~110	40	1.84	1.1±0.3
Mo067	Plasma etching	~110	60	1.27	2.1±0.8
Mo068	Plasma etching	~110	70	0.86	3.3±1.3
Mo070	Plasma etching	~280	0	2.46	0.8±0.2
Mo071	Plasma etching	~280	40	1.76	2.2±0.5
Mo072	Plasma etching	~280	60	1.32	3.2±1.3
Mo073	Plasma etching	~280	70	0.89	2.9±1.2
Mo076	Sand blasting	2-3 µm	0	0.85	1.3±0.3
Mo075	Sand blasting	2-3 µm	40	1.25	0.95±0.2
Mo074	Sand blasting	2-3 µm	60	1.92	0.5±0.2
Mo059	Sand blasting	2-3 µm	70	2.5	0.3±0.10

301

302

Table 1: *Exposure parameters for each individual sample. All samples were exposed to*

303

D ion beam with an energy of 1 keV/D at 300 K. We list here the sample naming, treatment of

304

the substrate surface, estimated surface roughness, angle of incidence of the D beam, the

305

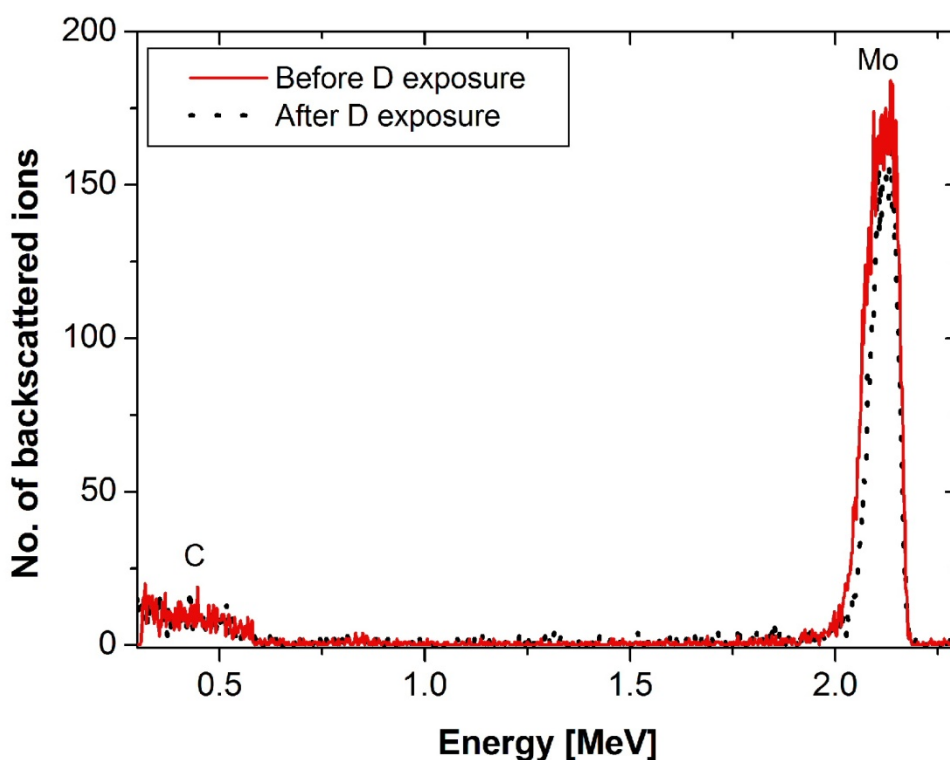
maximum fluence of the exposure spot where RBS analysis was performed and calculated

306

sputter yield as described in the text.

307

308 After the exposure of each series of samples to the D ion beam, they were
309 analysed by RBS. By comparing the measured Mo thickness profiles obtained by
310 RBS before and after exposure to the D beam, we can determine how much of the
311 material was eroded at a certain D ion fluence. An example of an RBS measurement
312 before and after D exposure is shown in Figure 6 where one sees a Mo peak at
313 around 2.1 MeV and RBS signal from the carbon bulk material at lower energies. It is
314 clearly visible that the Mo peak integral becomes smaller after the D ion irradiation
315 compared to the virgin sample. This shows that the Mo layer was considerably
316 eroded by the D ions.

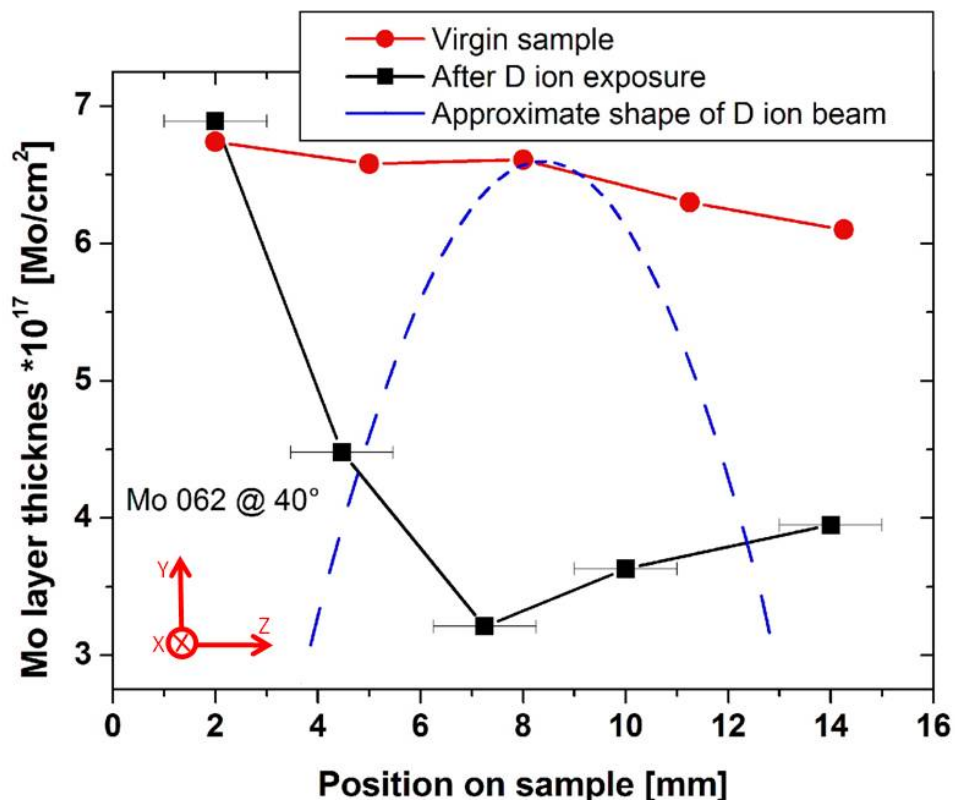


317

Figure 6: Spectra of RBS measurements of a Mo-coated graphite sample (roughness 5 nm) using 2.5 MeV ^4He ions, before and after the exposure to 1 keV/D ions at 0° in the middle of the erosion crater.

318 In Figure 7 we show the vertical profile scan of the nominal Mo layer thickness
319 before and after the D ion exposure as measured by RBS. We see that the thickness
320 of the virgin Mo layer is within 5 % of the nominal thickness of 115 nm or 7.4×10^{17}

321 Mo/cm², respectively. This number is only given as an orientation but since we were
 322 aware from previous experience that samples could have some variance in thickness
 323 and gradient along the sample, each sample was measured before the ion exposure.
 324 For this reason, we took for the sputter yield calculations as the initial thickness the
 325 value measured in the middle of the sample with the variation from few neighbouring
 326 positions. In addition to the RBS measurement, the Gaussian approximation of the
 327 beam profile is also shown in figure 7. The minimal nominal layer thickness after the
 328 D ion exposure coincides well with the maximum of the beam. In some cases, we
 329 observe some decrease in the Mo layer thickness outside the centre of the beam.
 330 We think this is due to D ion beam halo, which can be observed also on eroded a-
 331 C:H film, Figure 5a.



332
 333 *Figure 7: Thickness of the Mo layer as measured by RBS, before and after the exposure*
 334 *to 1 keV D ions at 40° impact angle on smooth sample with Ra~5 nm. The dashed line*
 335 *represents the envelope of the ion beam, approximated by a Gaussian fit of the Faraday cup*

336 measurements from Figure 5. The error bars on individual positions represent the error of
337 position between before and after exposure RBS measurement. Due to high fluence on this
338 sample $D_{max}=3.19 \times 10^{23} D/m^2$, the depression in erosion crater exceed the 50% of the
339 original Mo thickness.

340

341 The difference between the Mo areal density $n_{Mo(before)}$ of the initial layer and the
342 areal density $n_{Mo(after)}$ of the irradiated surface gives us the amount of eroded Mo
343 atoms. Sputtering is quantified via the sputtering yield, which is defined as:

344
$$Y_{Mo} = \frac{n_{Mo(before)} - n_{Mo(after)}}{D_{fluence-max}}.$$

345 $n_{Mo(before)}$ was taken as an average of five measurement points across the
346 sample, while $n_{Mo(after)}$ was taken at the minimum Mo thickness measured at the
347 bottom of the erosion crater (see Figure 7). In the centre of the sputtering crater we
348 have also estimated the maximum D ion fluence, marked as $D_{fluence-max}$. The value of
349 $D_{fluence-max}$ was calculated by multiplying the time-averaged D ion fluence as
350 measured during individual sample exposure, given in table 1, by the ratio of 2.7 and
351 cosine of the angle between sample surface normal and ion gun axis.

352 D irradiation and RBS analysis had to be conducted with two different sample
353 holders inside the INSIBA chamber. Therefore, the samples had to be transferred
354 from one holder to the other, which could result in the worst case to a mismatch of
355 measuring position fore ~ 1 mm, i.e., the maximum of the erosion crater is missed by
356 1 mm, while still the maximum of the D ion flux is used for calculating the sputter
357 yield. This corresponds to an overestimated $D_{fluence-max}$ by 15%, which translates to
358 underestimation of the sputtering yield by 15% at 0° impact angle and up to 30% at
359 high impact angles. Hence, we assume that the estimated mismatch gives us the
360 dominant contribution to the error bars for our absolute values of the sputtering
361 yields. To the error bars being due to the possible mismatch of the maximum erosion

362 crater we have added also the errors due to the RBS measurements statistics and
363 the discrepancy between the measurements and the simulation in the SIMNRA
364 software. This adds additional 5 % error to the calculated sputter yield. The dose
365 measurement is not included in the error since it is a systematic error and is
366 estimated to be about 5-10 %.

367 Figure 9 shows the sputter yield as obtained for the smooth surface with
368 $R_a \sim 5$ nm. We observe a clear increase of sputter yield with increasing angle of inci-
369 dence by roughly a factor of five at 70° as compared to 0° .

370 The experimental results for the all four investigated surface roughnesses are
371 presented in Figure 10, which shows the sputter yield as a function of impact angle
372 together with SDTrimSP-3D simulations for the specific surface roughness. For easi-
373 er comparison, the 5 nm roughness case is also shown in Figure 10a, the same data
374 as in Figure 9. For all the surfaces we observe a strong angular dependence of sput-
375 ter yield. Intermediate surface roughnesses, i.e. $R_a \sim 110$ nm and $R_a \sim 280$ nm, show
376 an increase of the sputter yield with the angle by a factor of approximately five com-
377 pared to 0° , reaching similar values as $R_a \sim 5$ nm. - For the smooth surface with $R_a \sim 5$
378 nm and the low roughness surface with $R_a \sim 110$ nm, there is no maximum observed
379 in the analysed angle range and the yield increases up to the highest measured im-
380 pact angle of 70° . For the surface roughness of $R_a \sim 230$ nm, the maximum of the
381 sputter yield is observed at 60° . For $R_a \sim 2-3$ μm there is no increase of sputter yield
382 for large angles but it attains its maximum at 0° . The sputter yield at 0° shows an in-
383 crease with surface roughness from 0.5×10^{-2} Mo/D for the low values of R_a to
384 1.3×10^{-2} Mo/D for the roughest surface. The sputter yield at large angles, e.g. at 60° ,
385 increases with the surface roughness except for the case of h highest roughness
386 studied, where it attains the lowest value.

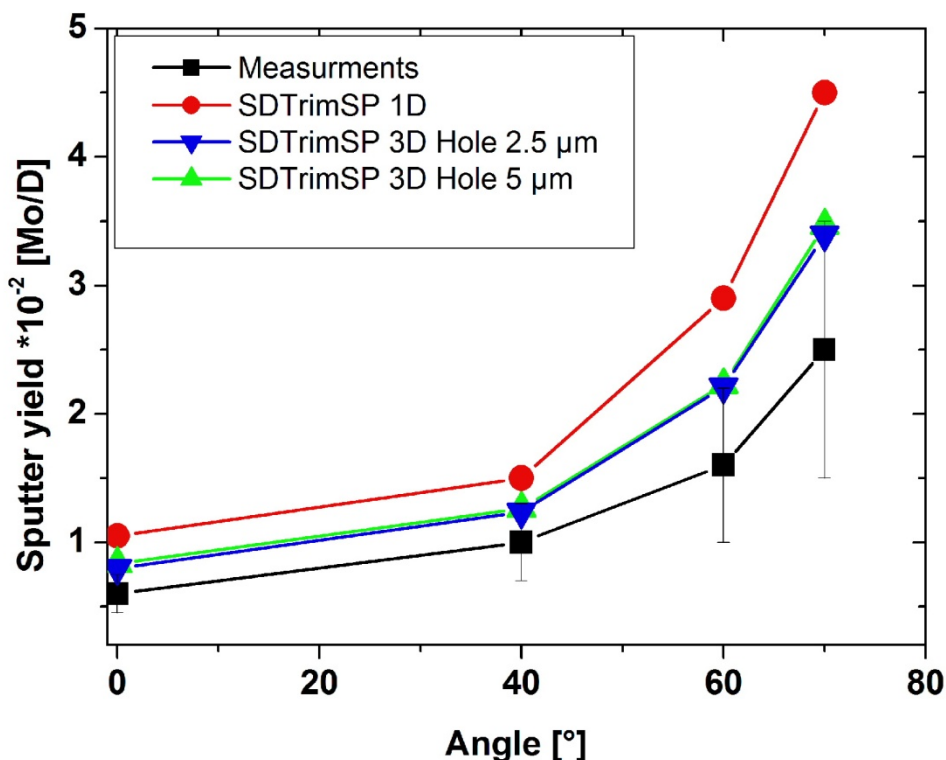
387

388 5.2 Simulation results

389 Figure 8 also includes the results obtained by applying the semi-analytical fit
390 formula from [2] and simulated data computed by SDTrimSP-1D [17] and -3D [9].
391 The semi-analytical formula is only valid for smooth surfaces. The input parameters
392 used are: $f=1.66$, $b=0.328$, $c=1.015$, $Y(E_0,0)=0.015$. The parameters were extrapo-
393 lated from Table 20 in *R. Behrisch and W. Eckstein* [2], as there are no parameters
394 for a D ion energy of 1 keV on Mo. Simulations by SDTrimSP were performed with
395 10^6 projectiles. Surface binding energy E_s was set to 8.45 eV. The heat of sublima-
396 tion ΔH_s is a first-order approximation for E_s being 6.81 eV [16]. Comparisons of cal-
397 culated and measured energy in literature have led to argue that, at least in the case
398 of Mo, E_s is larger than the heat of sublimation [16]. For this reason, an average val-
399 ue of the surface binding energies for different surface orientations, as they range
400 from 7.38 eV up to 9.18 eV [16], was used in the calculation. A lower value of sur-
401 face binding energy leads to higher values of sputter yield for all angles.

402 One of the main input for SDTrimSP-3D is the morphology of the surface. This
403 information was derived from AFM ($R_a \sim 110$ nm and 280 nm) as well as CLSM
404 ($R_a \sim 2-3$ μm) measurements. However, for the samples with $R_a \sim 5$ nm, the observed
405 holes (artefacts of polishing as discussed in sample preparation section) could not
406 be measured accurately with the AFM, since the depth of the holes is larger than the
407 dynamic range of the AFM. Therefore, the input surface for SDTrimSP was con-
408 structed as smooth surface with one cubic depression with dimensions of
409 $2.5 \times 2.5 \times 2.5$ μm^3 , on the 10×10 μm^2 grid, thus creating an uniform distribution of
410 holes on simulated surface. Such a construction matches the surface morphology
411 observed by SEM and produces good agreement of the SDTrimSP-3D calculated
412 sputter yield with the measured ones. We also tried the simulation with different hole
413 dimension, as seen on **figure 8**, which yielded similar absolute values of the sputter
414 yield. Thus, we did not proceed further with simulation of uneven distribution of hole

415 size. This construction was chosen because using only AFM data as input for the
416 surface structure could not reproduce the surface.
417
418



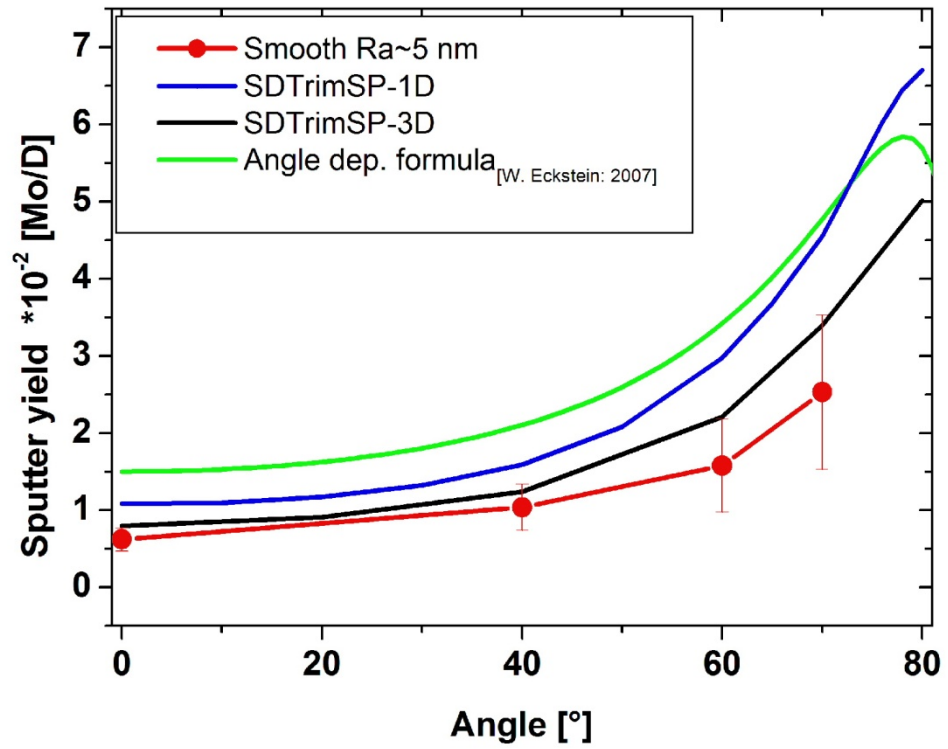
419

Figure 8 Angular dependence of the Mo sputter yield for 1 keV D particles for samples with $R_a \sim 5$ nm. Additional to the experimental values, the yields obtained with SDTrimSP 6.0 code [17] and with SDTrimSP-3D [9]. For SDTrimSP-3D we plotted the simulations for holes of 2.5 μm and 5 μm .

420 Comparison of the SDTrimSP-3D simulated data with experimentally measured data
421 shows that simulations give slightly higher values of the sputter yields, but are still
422 within the experimental error bars. Also the semi-analytical formula and SDTrimSP-
423 1D lead both to larger values as compared to the experimental data. However, all
424 three approaches agree on the trend of the sputter yield dependence on the impact
425 angle, namely that the sputter yield increases drastically for angles above 50°.

426 The simulation data obtained from SDTrimSP-3D for all the studied surface
427 roughnesses are shown in figure 10. For intermediate surface roughness, we did not
428 observe this micron-size holes as seen on polished samples. Therefore, we did not
429 include additional holes in calculations for other surface roughnesses. We are sus-
430 pecting that plasma etching procedure to smoothens out the holes to some extent.
431 The trend of the simulated sputter yield with increase of the angle agrees with the
432 experiment for the surface roughness of 110 nm. In the case of 280 nm surface
433 roughness, the simulation does not show any peak of sputter yield at 60° as is ob-
434 served in experimental data but just increases with angle as for the other two cases
435 before. The simulation for the roughest surface of 2-3 μm predicts an increase of the
436 sputter yield by a factor of 1.5 at the largest angle, while the experimental data show
437 a decrease of the sputter yield by a factor of five. The absolute values of the simulat-
438 ed sputter yield at 0° are in all cases higher than in the experiment except for the
439 roughest case.

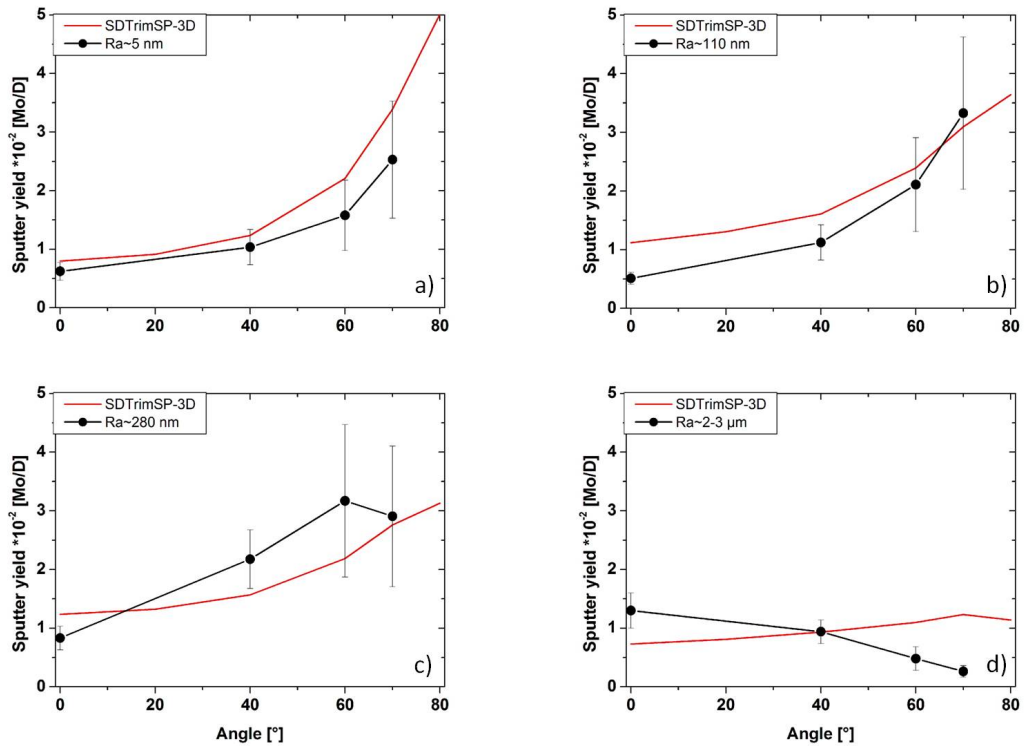
440



441

Figure 9: Angular dependence of the Mo sputter yield for 1 keV D particles for samples with Ra~5 nm. Additional to the experimental values, the yields obtained with SDTrimSP 6.0 code [17] and with SDTrimSP-3D [9] as well as the ones from a calculation using the Eckstein angular formula [2] for ideal smooth surfaces are given.

442



443

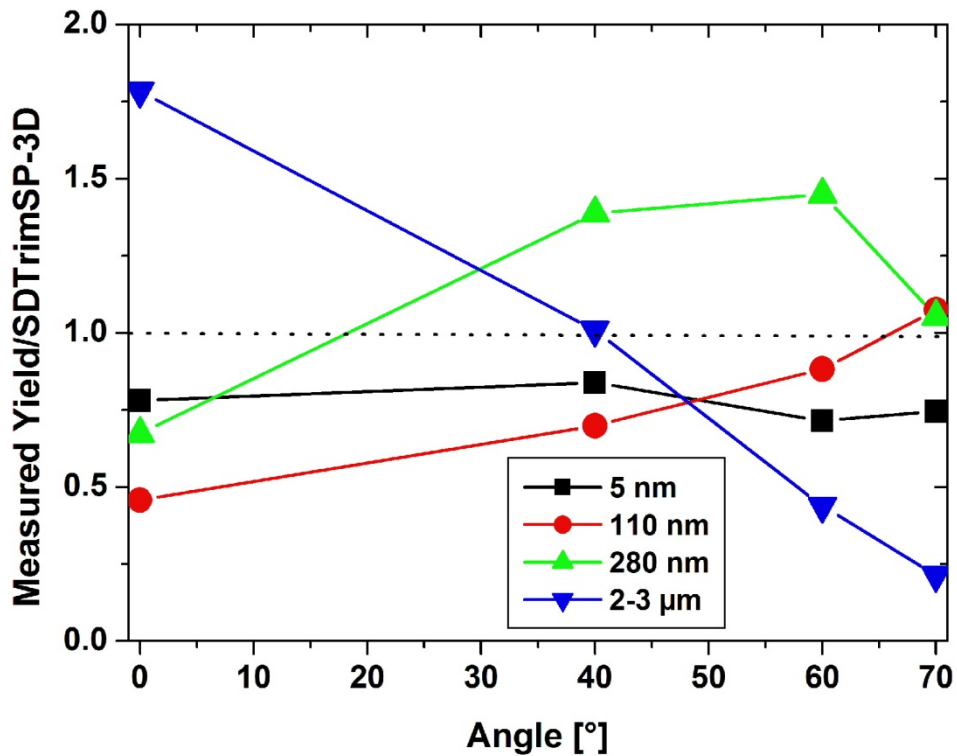
Figure 10: The experimental sputter yield and the SDTrimSP-3D simulation results as a function of angle for 1 keV D on Mo for the four different studied surface roughness with Ra a) ~5 nm, b) ~110 nm, c) ~280 nm and d) ~2-3 μm.

5.3. Discussion

444 We will first discuss the quality of the agreement between the experiment and
 445 the simulation. Second discuss the possible reason for disagreement of both data. In
 446 Figure 11 we show the relative values of the measured sputter yield divided by the
 447 values calculated with SDTrimSP-3D. If simulations are in total agreement with the
 448 measurements, we expect flat lines in the vicinity of 1. This is the case for the
 449 smoothest samples with Ra~5 nm, obtaining almost perfect agreement with only
 450 systematically overestimating the simulated sputter yield. With increasing surface
 451 roughness a larger deviation between simulation and experiment is observed.
 452 However, except for Ra~2-3 μm, the general trend with angle of incidence can be
 453 seen in both cases.

454 In general, the SDTrimSP-3D calculations give larger values as measured. For
455 the case of the samples with $R_a \sim 2-3 \mu\text{m}$, larger discrepancies between the
456 calculated and the measured data can be noticed. As shown for the case of
457 SDTrimSP-3D calculations for smooth surfaces, we needed to introduce the surface
458 with holes to calculate the sputter yields. As compared to the 1D model, the
459 introduction of holes significantly decreases the sputter yield [18]. The surfaces for
460 the roughest samples also show some deep depressions in the surface morphology
461 and these were fed in SDTrimSP-3D as input. This is one of the possible reasons to
462 obtain lower values of sputter yield. Additionally, SDTrimSP-3D does not take into
463 account spikes smaller than the lateral resolution of the input data. In our case this
464 means no additional features smaller than 650 nm. From SEM images, seen on
465 figure 2, we observe structures, with smaller R_a , on top of the rough surfaces. The
466 erosion of these spikes-like structures can explain the larger values measured at 0°
467 impact angle compared to simulations. In addition, these structures increase the
468 active surface of the sample. This leads to a larger prompt deposition rate at higher
469 impact angles, which is experimentally observed as a decrease of the sputter yield.
470 From SDTrimSP data we can estimate that this prompt deposition can occur for up
471 to 25% of sputtered atoms. However, the exact value is strongly dependent on
472 surface roughness and impact angles. Despite this the SDTrimSP-3D can still be a
473 useful tool to predict the behaviour of the sputter yield. However, we need to be
474 aware of its limitations posed by the quality of the provided input data, provided with
475 CLSM.

476



477

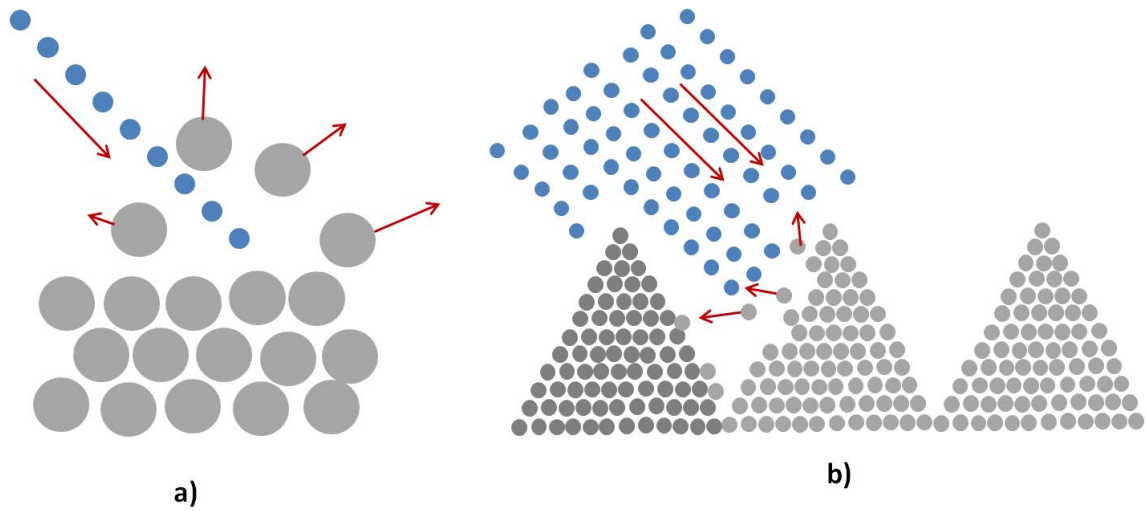
Figure 11: Measured values of the sputter yield divided by the SDTrimSP-3D calculated values. As observed in most of the cases the SDTrimSP-3D calculation of the sputter yield is higher than the experimentally obtained sputter yield.

478

479 From the presented data we can observe that the surface roughness
 480 influences the sputter yield differently at small and large impact angles. Let us first
 481 consider large incidence angles. For the polished samples and samples of
 482 intermediate roughness, we can see an increase of the sputter yield with increasing
 483 impact angle, dominantly for angles beyond 40°. This trend is also supported by
 484 SDTrimSP-3D simulations. As for angles between 0-40° we do not have data, it is
 485 only a speculation how sputter yields behave in this range. The increase of sputter
 486 yield with higher impact angles can be easily explained by the fact that more
 487 momentum is transferred to target atoms in the forward direction. Therefore, the
 488 probability of atoms escaping from the surface increases at larger impact angles.
 With such a model we would see the maximum sputter yield for smooth surfaces at

489 angles approaching 90° , which is also supported by theoretical prediction of Eckstein
490 [2]. As the surface roughness increases, more of the surface elements are exposed
491 at effectively larger angles (90°). The consequence of the change of the effective
492 impact angle with increasing roughness can be observed by the fact that the
493 steepness of the angular dependence the sputter yield is decreasing, as observed by
494 the experiment and confirmed by simulation.

495 When we increase the surface roughness to larger values, two additional
496 processes start to affect the sputtering process. The first process is local
497 redeposition of sputtered atoms on the nearby surfaces. This increases the
498 probability of a sputtered atom remaining on the surface, which decreases the
499 measured sputter yield. From our design of the experiment, we only detect the atoms
500 sputtered away from the target and none of the sputtered atoms that are promptly
501 redeposited at the surface. The second process is that the increase of surface
502 roughness also leads to shadowing effects, which are more pronounced at higher
503 impact angles. Therefore, less sample surface is exposed to the irradiating D beam,
504 which leads to a corresponding decrease of the sputter yield. An illustration of these
505 two processes is schematically shown in Figure 12. From our results we assume that
506 these two effects are most pronounced for the samples with the highest surface
507 roughness (2-3 μm). To make clear conclusions, more intermediate roughness
508 values should be investigated. In any case, we see that the sputter yield is
509 significantly decreasing for higher impact angles as compared to 0° impact angle for
510 rough samples.



511

512 Figure 12: *Schematic representations of the processes competing and providing the*
 513 *angular and roughness dependence of the sputter yield. a) Transfer of momentum in lateral*
 514 *direction at higher impact angles for smooth surfaces. b) Rough surfaces increase*
 515 *redeposition of sputter atoms and shadowing of surfaces.*

516

517

518

519

520

521

522

523

524

525

526

527

528

529

Now let us discuss about the discrepancy in the sputter yield between the measured and the simulated values at low impact angle where we also measured a small increase with surface roughness for surface roughnesses of ~280 nm and ~2-3 μm . A similar behaviour of the absolute sputter yield values compared to SDTrimSP simulations for different surface roughness was observed by Arredondo et al. [5]. They also report an increase of the sputter yield at low impact angles ($<40^\circ$) with increasing surface roughness and decrease at high impact angles ($>40^\circ$). It is important to stress that the rough surfaces prepared in that experiment had a much wider angular distribution of surface angles compared to the samples in our study, although they still had a Ra value of 20 nm. This angular distribution in case of Arredondo et al. [5] is assumed to be the origin of the lower sputtering yield at 60° impact angle compared to the smooth surface, despite the low Ra value. We observe an increase of the sputtering yields for intermediate roughness. One of the most

530 important issues raised by R. Arredondo et al. [5] is the observed discrepancy of
531 calculated sputter yields with SDTrimSP [9] for D on W, where SDTrimSP
532 overestimated the sputter yield approximately by a factor of two. The explanation
533 given by Arredondo et al. [5] is that the binary collision approximation, on which
534 SDTrimSP code is based on, is not strictly satisfied for brittle materials (W, Mo),
535 in contrast to ductile ones (Ni, Au). We observe a similar overestimation for D on
536 Mo, where the simulated or literature data [2] exceed the measured sputter yield,
537 Figure 9. The agreement between experimental data and SDTrimSP-3D
538 simulations was improved by taking a higher surface binding energy and
539 appropriate surface morphology data. With this the simulations achieved better
540 agreement with the measured data.

541

542 **6. Conclusion**

543 The aim of this work was to investigate the effect of surface roughness and
544 morphology on the sputter yield of Mo. To this end a series of Mo thin film samples
545 of varying surface roughness were exposed to D_3^+ ions with 1 keV/D ions at room
546 temperature under different impact angles ranging from 0 to 70°. The experimental
547 results were compared to SDTrimSP 1D and 3D simulations.

548 The data obtained in this study reveal that there is a clear influence of the inci-
549 dence angle and surface roughness on the sputter yield of Mo. For polished surfaces
550 we observed an increase of the sputter yield at higher impact angles, as predicted by
551 theory. With increasing surface roughness, the sputter yield increases at 0° impact
552 angle. For higher impact angles we observe two different behaviours: if the surface
553 roughness is in the medium range experimentally investigated (a few hundreds of
554 nm), the dominant effect is that more and more surface is exposed to higher impact
555 angles leading to correspondingly increasing sputter yield. However, for the very
556 rough surfaces a decrease of the sputter yield at high impact angles was observed

557 which we explained by redeposition and shadowing effects of the rough surface. As
558 we showed, this decrease is only observed on surfaces with the highest surface
559 roughness of 2-3 μm .

560 In general, the calculation with SDTrimSP-3D qualitative produce good agree-
561 ment with measured angular and roughness dependence of sputter yield. However,
562 there are still discrepancies between the absolute calculated values of sputter yield
563 with SDTrimSP-3D code and measured values. The possible reason for this is the
564 lack of necessary detail in surface reproduction which is not possible with current
565 methods but a necessary input for SDTrimSP-3D. Therefore, we infer that for now it
566 is more advisable to take experimental data for PFC design works on surfaces as
567 they more closely resemble the real components.

568 The simulated conditions of irradiation with mono-energetic D and fixed angles
569 represent a compromise between well-characterised ion beam and real conditions in
570 a thermonuclear reactor, where we have a broader distribution of particle energies
571 and also the local magnetic field exerts a strong influence on the effective impact
572 angle [16]. Still, the obtained data serve as a valuable guideline for the design of
573 plasma-facing component surfaces in tokamaks and for estimating their lifetime.
574 Strictly from the erosion point of view, the components with high value of Ra will last
575 longer than smooth ones.

576

577 **Acknowledgments**

578

579 This work has been carried out within the framework of the EUROfusion
580 Consortium and has received funding from the Euratom research and training
581 programme 2014-2018 under grant agreement No 633053. Work was performed
582 under EUROfusion WP PFC. The views and opinions expressed herein do not

583 necessarily reflect those of the European Commission. The authors acknowledge the
584 support from the Slovenian Research Agency (research core funding No. P2-0405).

585

586 **References**

587 [1] R. Chodura, Journal of Nuclear Materials. 111 (1982) 420-423

588

589 [2] W. Eckstein. Sputtering yields. In R. Behrisch and W. Eckstein, editors, Sputtering by Particle
590 Bombardment IV, volume 110 of Topics in Applied Physics, chapter Sputtering Yields, pages 33–187.
591 Springer Berlin Heidelberg, Berlin, 2007.

592

593 [3] M. Küstner et al. Nuclear Instruments and Methods in Physics Research B 145 (1998) 320

594

595 [4] M. Küstner et al. Journal of Nuclear Materials 265 (1999) 22

596

597 [5] R. Arredondo et al. Nuclear Materials and Energy 18 (2019) 72

598

599 [6] R. Stadlmayr et al. Instruments and Methods in Physics Research B 430 (2018) 42

600

601 [7] G. F. Matthews et al. Physica Scripta T145 (2011) 014001

602

603 [8] R. Stadlmayr et al. Physica Scripta T171 (2020) 014021

604

605 [9] U. von Toussaint et al. Physica Scripta T170 (2017) 014056

606

607 [10] E. Vassalo et al. Thin Solid Films 603 (2016) 173

608

609 [11] Mayer M 1997 *SIMNRA User's Guide, Report* IPP 9/113, Max-Planck-Institut für
610 Plasmaphysik Garching (www.rzg.mpg.de/~mam/)

611

612 [12] S. Markelj et al. Nuclear Fusion 59 (2019) 086050

613

614 [13] S. Markelj et al. Nuclear Materials and Energy 12 (2017) 169–174

615

616 [14] IonEtch specification, <https://tectra.de/wp-content/uploads/2017/03/IonEtch.pdf> (26.05.2020)

617

618 [15] B. M. Berger Nuclear Materials and Energy 12 (2017) 468

619

620 [16] W. Eckstein, Computer Simulation of Ion-Solid Interactions, Springer Series in
621 Material Science, Vol. 10, Springer Berlin, Heidelberg 1991

622

623 [17] A. Mutzke et al. SDTrimSP Version 6.00. IPP 2019-02, Max-Planck-Institut für Plasmaphysik
624 (Ed.) https://pure.mpg.de/rest/items/item_3026474_2/component/file_3026477/content, 2019

625

626 [18] A. Mutzke, Personal communication 2020

627

628

629 Author creditship:

630

631 **M. Kelemen:** Conceptualization, Methodology, Writing-Original Draft, Investigation **T. Schwarz-**

632 **Selinger:** Conceptualization, Writing - Review & Editing **A. Mutzke:** Software, Resources **M. Balden:**

633 Resources, Investigation, Writing - Review & Editing **E. Vassallo:** Resources, Writing - Review &

634 Editing **M. Pedroni:** Resources **D. Dellasega:** Resources, Writing - Review & Editing **M. Passoni:**

635 Resources **F. Romeo:** Resources **A. Hakola:** Conceptualization, Writing - Review & Editing **P. Peli-**

636 **con:** Resources **R. Zaplotnik:** Resources, Investigation **S. Markelj:** Conceptualization, Methodology,
637 Writing-Original Draft, Investigation, Writing - Review & Editing